The International Journal of Advanced Manufacturing Technology (2020) 107:3277–3297
https://doi.org/10.1007/s00170-020-05242-9

ORIGINAL ARTICLE

Mechanical characterization of aged AA2026-AA2026 overcast joints fabricated by squeeze casting

Muhammad Asad Ali[1,2] · Kashif Ishfaq[2] · Muhammad Huzaifa Raza[1] · Muhammad Umar Farooq[2] · Nadeem Ahmad Mufti[2] · Catalin I. Pruncu[3,4]

Received: 1 January 2020 / Accepted: 23 March 2020 / Published online: 14 April 2020
© The Author(s) 2020

Abstract

Squeeze overcasting has emerged as an attractive option for casting of Al alloys in terms of mechanical properties. The attainment of the desired magnitude of these properties is challenging in overcasting due to the involvement of a number of process parameters. In this study, the effects of insert preheat temperature (T_I) along with pouring temperature (T_P), and squeeze pressure (P_S) on the mechanical properties of squeeze overcast AA2026-AA2026 joint were investigated. Experimental results revealed that the squeeze pressure is the most prominent factor affecting the ultimate tensile strength (UTS) while micro-hardness (MH) is significantly influenced by the pouring temperature. Maximum values of UTS (315 MPa) and MH (130 HV) were achieved at a P_S of 120 MPa, T_P of 780 °C, and T_I of 250 °C. Energy dispersive X-ray (EDX) analysis witnessed that T_I has also a significant role in determining the quality of bond between the substrate and the melt. Scanning electron microscopy (SEM) depicts that the morphology of the fractured surface has a sound influence on both selected responses. Both the strength and hardness are noticed better if the fractured surface possesses the flat-faced morphology. Furthermore, an empirical regression model was developed using response surface methodology (RSM) design and validated through eight confirmatory experiments. RSM integrated multi-objective optimization genetic algorithm (MO-GA) was deployed to optimize the UTS and MH. The comparative results obtained from RSM and MO-GA demonstrated that the deviation in experimental and predicted values is less than 5%.

Keywords 2026 Al alloy · Aging · Insert preheat temperature · Mechanical properties · Response surface methodology

1 Introduction

Aluminum alloys are widely used in aerospace, transportation, and automotive industries due to their high strength, low density, and better corrosion resistance. Especially, the use of wrought aluminum (2xxx) series is quite significant in the above-mentioned industrial sectors [1]. Typically, the applications of the said material category require the use of casting as a primary process. However, the properties exhibited by these alloys mainly depend on the casting technique and the process parameters used for their development [2]. Manufacturing of high-performance materials at a competitive cost is now the essential demand of industry for their survival in this competitive environment. Among the different options, overcast manufacturing seems to be an attractive alternative [3, 4]. But in overcast manufacturing, the desired properties can only

✉ Catalin I. Pruncu
c.pruncu@imperial.ac.uk

Muhammad Asad Ali
asad.ali@uet.edu.pk

Kashif Ishfaq
kashifishfaq1@gmail.com

Muhammad Huzaifa Raza
huzaifaraza4@gmail.com

Muhammad Umar Farooq
muf@uet.edu.pk

Nadeem Ahmad Mufti
namufti@uet.edu.pk

[1] Department of Industrial Engineering, University of Engineering and Technology Taxila, Taxila 47080, Pakistan

[2] Department of Industrial and Manufacturing Engineering, University of Engineering and Technology Lahore, Lahore 54890, Pakistan

[3] Department of Mechanical Engineering, Imperial College London, London SW7 2AZ, UK

[4] Mechanical Engineering Department, University of Birmingham, Birmingham B15 2TT, UK

be achieved if a suitable joining technique is selected. Appropriate selection of joining technique is crucial to warrant the attainment of desired mechanical characteristics. Numerous techniques have been used by the researchers for joining similar and dissimilar metals. These techniques are mainly classified into three categories: (A) solid-solid bonding, like explosive welding [5], laser welding [6], friction stir welding [7], hydrostatic extrusion [4], brazing [8], and rolling [9]; (B) solid-liquid bonding, for instance, overcasting [10, 11] and hot dipping [12]; (C) liquid-liquid bonding, such as direct chill casting [13], lost-foam casting [14], and continuous casting [15]. It is worth mentioning that solid-solid bonding is time consuming and costly due to the shape and design constraints of the substrate. Liquid-liquid bonding is not economically feasible. Hence, it is not a preferable choice in industrial applications [16].

On the other end, solid-liquid bonding which is also known as overcasting or compound casting has gained significant attention owing to its higher production efficiency and low operational cost [17]. In this technique, liquid metal is brought into contact with the solid metal substrate. In this way, a continuous metallic transition zone is formed between the two metals by diffusion reaction. Overcasting has been used for a variety of similar and dissimilar material systems such as Mg-Mg [18], Al-Al [11, 19], Al-Mg [20, 21], Al-Cu [10], and Fe-Cu [22]. However, in the case of Al-Al joint, the formation of Al_2O_3 film makes the overcasting onerous because Al_2O_3 film is thermodynamically stable and limits its wettability with

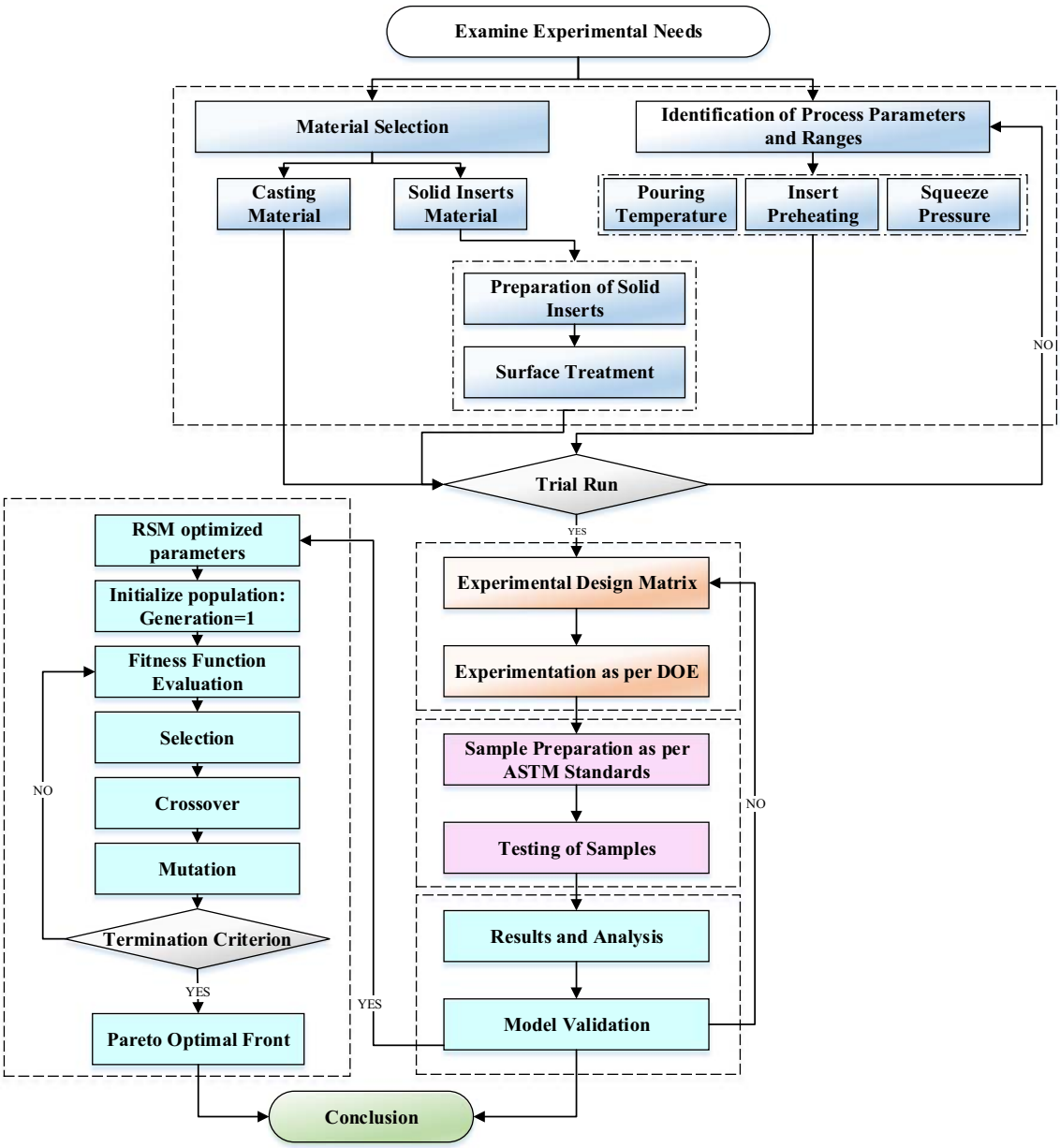

Fig. 1 Research methodology

the melt [17]. Therefore, zinc coating on the solid metal substrate has been introduced by the researchers which has comparatively low melting temperature and makes the diffusion easy during overcasting [18, 23]. Zn coating protects the surface of solid insert substrate from oxidation and enhances the wettability among the molten metal and solid insert material [24, 25]. It has been reported that macro cracks and porosities are formed at the interface region because of improper diffusion of melt and solid insert during overcasting [16]. These defects cannot be minimized by only controlling the melt temperature. At low temperature, weak metallurgical bond is formed whereas high temperature causes a severe melting of the insert material. It has been cited by the researchers that the squeeze casting process is a viable option to address the aforesaid issues as it can improve the metallurgical bonding of overcast joints [26, 27]. Moreover, the inherent defects like hot tears and shrinkage cavities are significantly reduced under high pressure [28–30]. The squeeze casting process has been used for the compound casting of various similar and dissimilar metals, for instance, AA6101-AA6101 [31], A356-AA6101 [32], and Mg (AM60)-A390 [33].

In previous studies, a significant number of researchers have analyzed the influence of various squeeze casting input parameters on the strength and other mechanical properties of over-casted joints. Liu et al. [10] used pouring temperature and squeeze pressure as input parameters to investigate their effects on tensile strength, hardness, and microstructure of Al-Cu overcast joints. In addition to pouring temperature and squeeze pressure, Liu et al. [32] have also considered surface treatment as an input parameter for A356-AA6101 in another study. Their results indicate that mechanical properties and microstructure were significantly affected by squeeze pressure, pouring temperature, and surface treatment. In another work, the effects of T6 heat treatment on grain structure were investigated during squeeze overcasting of A356-AA6101 [34]. It was claimed that T6 heat treatment widens the transition zone that promotes the homogeneous diffusion of both metals. This eventually led to an increase in micro-hardness and shear strength of the joint. In another study, it was reported that appropriate heat treatment employment enhanced the bonding strength in compound casting [25]. Ali et al. [19] analyzed the effects of die temperature, squeeze pressure, and pouring temperature on the mechanical properties of 2024-2024 Al alloy overcast joints. Li et al. [35] found that pouring temperature had a prominent impact on the interface among Al and Mg. It is evident from the literature that squeeze pressure and pouring temperature are the most effective and repeatedly considered input parameters for mechanical properties and microstructure in the squeeze casting process [29, 36, 37]. However, the effects the preheat temperature of solid insert in overcasting are yet to be thoroughly investigated.

Although there is an increased number of aluminum alloys used for overcasting, Al (2xxx) series need to be further explored due to their vast applications in critical industries. Extensive survey of literature revealed that limited research was conducted on AA2026 alloy using squeeze overcasting process which is mainly focused on the present research, even if the influence of various parameters has not been comprehensively inspected so far for the selected alloy during the overcasting process. Specifically, the effect of insert preheat temperature and aging on mechanical properties is still unexplored. The aspect of mathematical modeling of control variables with the mechanical characteristics has also been not discussed yet for the selected material during overcasting. Therefore, in this study, the effect of key control parameters like aging, pouring temperature, insert preheat temperature, and squeeze pressure is thoroughly investigated on the mechanical properties of squeezed AA2026-AA2026 overcast joint. Experimentation has been planned under the response surface methodology experimental design technique. The experimental results are explained using SEM micrographs and EDX analysis to have an insight into the process physics. Furthermore, mathematical relations of control variables with the mechanical attributes of the overcast joint have been formulated and validated, while the genetic algorithm (GA) has been employed for multi-objective parametric optimization. The optimized set of parameters has also been achieved that warrants the optimal values of the responses.

Table 1 Chemical composition of the alloy (AA2026) used for experimentation

Elements	Cu	Zr	Mg	Zn	Ti	Si	Fe	Mn	Al
Wt.%	3.91	0.09	1.23	0.1	0.04	0.06	0.08	0.72	93.77

2 Materials and methods

As mentioned in the previous section, the primary objective of this research is to evaluate the impact of key squeeze overcasting parameters on the mechanical properties of the Al-Al overcast joint. The work was organized in a systematic manner to avoid any discrepancy. The hierarchy of the present research contains different

Table 2 Input parameters with selected levels

Input parameters	Units	Levels		
		Low (−1)	Medium (0)	High (+1)
Pouring temperature (T_P)	°C	730	780	830
Insert preheating (T_I)	°C	200	250	300
Squeeze pressure (P_s)	MPa	60	90	120

steps that were introduced in Fig. 1. As a first step, the workpiece and insert material were finalized. Aluminum alloy 2026 was selected for both the melt and solid insert material in the overcasting process. Chemical composition of the material was verified prior to experimentation via optical emission spectroscopy, and its

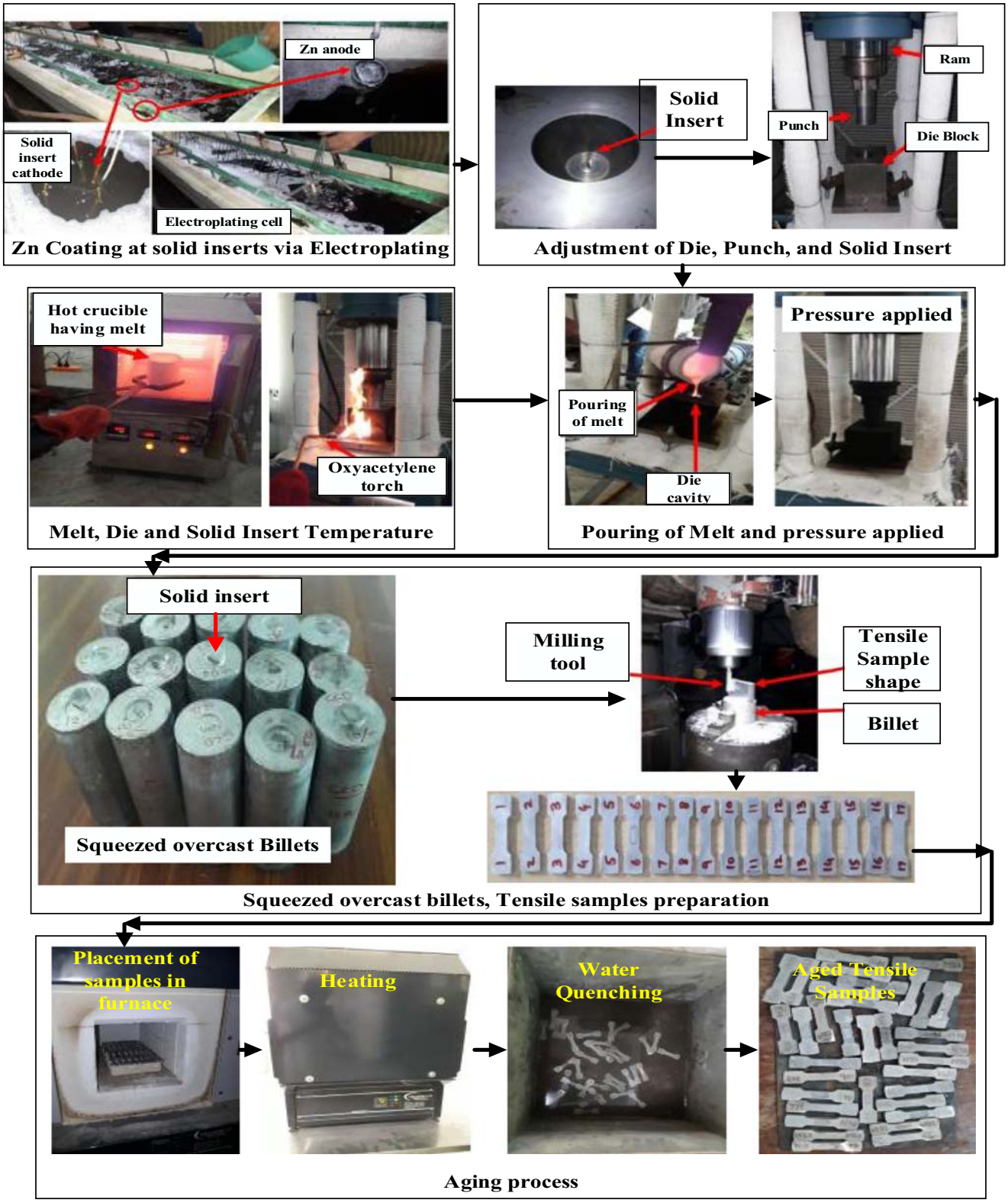

Fig. 2 Experimental flow diagram (squeeze overcasting process, tensile sample preparation, and aging process)

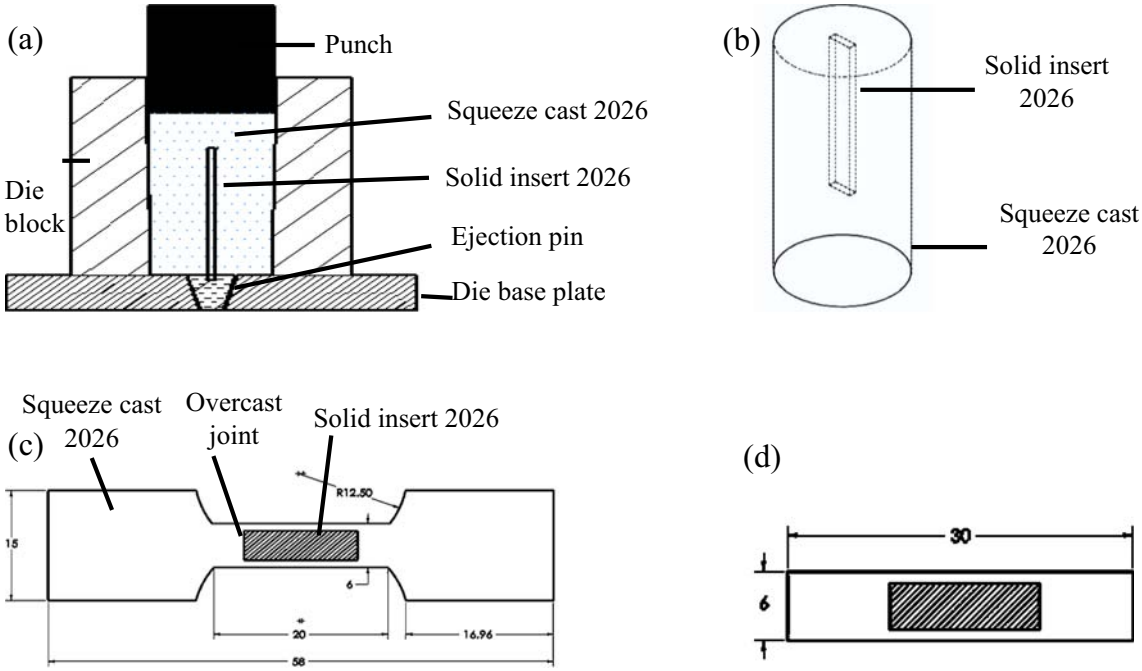

Fig. 3 Schematic illustration of **a** squeeze overcasting, **b** casted billet, **c** tensile sample, and **d** hardness sample

details are provided in Table 1. After ensuring the material's composition, solid inserts were machined. Rectangular bars of 4 × 13 × 90 mm were prepared for preliminary as well as mature trials.

To make the insert's surface smooth and burr free, abrasive papers were used. Afterwards inserts were chemically treated to make the surface free from any dust, lubricants, and oxides in the following steps: (1) degreasing by using C_3H_6O chemical at ambient temperature for 5 min, (2) alkali etching through NaOH solution (100 g/l, pH > 13) for 1 min at 55 °C, (3) acid pickling in 50% HNO_3 at room temperature for 30 s. Before each step of surface cleaning, water rinsing of solid inserts was done. After careful cleaning of insert surface, zincate treatment was employed at solid inserts for zinc coating. For efficient bonding of melt and solid insert during overcasting, Zn coating presence is compulsory [10, 31]. It is pertinent to mention that the thickness of coating layer is also an important consideration for determining the strength of the bond between the solid insert and melt. If the zincate layer is very thin of about 200–300 nm, it will not provide better bond strength [38], because such a small thickness of the layer is not sufficient for bonding as there is the possibility that zinc layer may evaporate when it comes in contact with the melt [26]. Therefore, it is required to increase the coating layer thickness, so that it can sustain itself during the bonding process. To increase the thickness of the zincate layer up to 7 μm [19, 39], zinc electroplating was performed on solid inserts by placing them in an electroplating cell.

Upon completion of the electroplating process, preliminary trials were performed. In the literature, it is stated that the mechanical properties and microstructure of Al-Al alloy overcast joint during squeeze overcasting process are influenced by pouring temperature and squeeze pressure [10, 19, 31, 32]. Therefore, both the said parameters were considered as input variables in the present research. Beside these parameters, the effect of insert preheat temperature was also investigated in this study, which is not explored yet. The insert

Table 3 Design matrix and measured responses

Run No.	Input parameters			Responses	
	T_p °C	T_I °C	P_S MPa	UTS MPa	MH HV
1	730	200	90	270.0	113.9
2	780	200	60	268.5	125.3
3	780	300	120	315.9	130.0
4	780	250	90	310.2	129.4
5	780	300	60	288.6	116.0
6	830	300	90	297.9	116.9
7	730	250	60	255.0	118.2
8	830	200	90	277.3	124.6
9	780	250	90	311.9	129.3
10	730	250	120	301.5	122.7
11	830	250	120	296.7	127.5
12	730	300	90	280.0	118.5
13	780	250	90	308.2	129.5
14	780	250	90	309.9	129.0
15	780	250	90	311.4	128.4
16	780	200	120	299.7	124.0
17	830	250	60	272.9	119.1

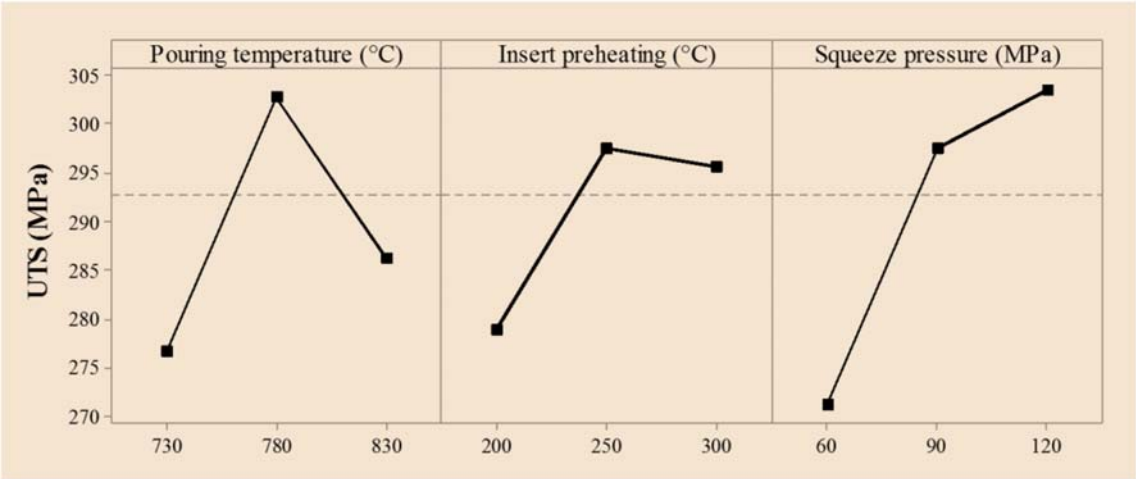

Fig. 4 Main effects plot for UTS

preheat temperature range was selected in such a way that the zinc layer may not be affected during the pouring of melt. Considering the aforementioned input variables, pilot experimentation was done to determine the levels of control variables. Those levels were selected for mature experimentation that can assure defect-free casting. Input parameters with their levels have been provided in Table 2.

For squeeze overcasting, A2026 alloy was melted in an electric furnace having a heating capacity of 1200 °C. At the same time, solid zinc-coated insert also was preheated according to the selected temperature range in another furnace. The die made up of H13 forged steel was heated (250 °C) using oxy-acetylene torch before pouring the molten metal. Die inner temperature was measured with an infrared thermometer. Before pouring the melt, solid insert and ejection pin were fitted in the base plate of the preheated die. Molten metal was poured in the metallic die at the required pouring temperature. Pressure was applied with the vertical hydraulic press of 100-ton capacity. Desired level of pressure was maintained until solidification of the melt. Pressure was released upon solidification, and billet was removed from the die. Billets with a size of 140 mm height × 61 mm diameter were obtained at the end. From each of the billet, two tensile and two hardness samples were extracted using a milling machine accordingly to ASTM standard E8/E8M-11. Influence of input parameters of squeeze overcasting was investigated on ultimate tensile strength and hardness. Then aging treatment was employed at squeeze overcast samples to obtain better UTS and hardness [17, 19, 40]. Aging treatment of samples were involved following three steps: (1) solution treatment in a furnace at 500 °C for 2 h, (2) cold water quenching of samples, and (3) artificial aging in a furnace at 170 °C for 2.5 h. Experimental flow diagram (squeeze overcasting process, tensile sample preparation, and aging process) were provided in Fig. 2. Schematic illustrations of squeeze overcasting, casted billets, tensile, and hardness samples have been presented in Fig. 3.

The selection of an experimental design is a crucial consideration for research as it ultimately determines the

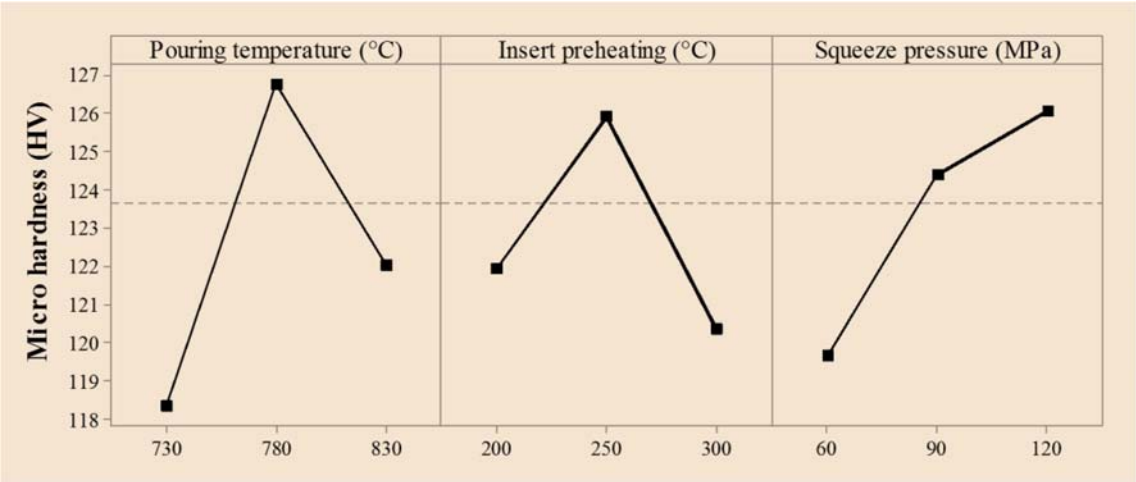

Fig. 5 Main effects plot for MH

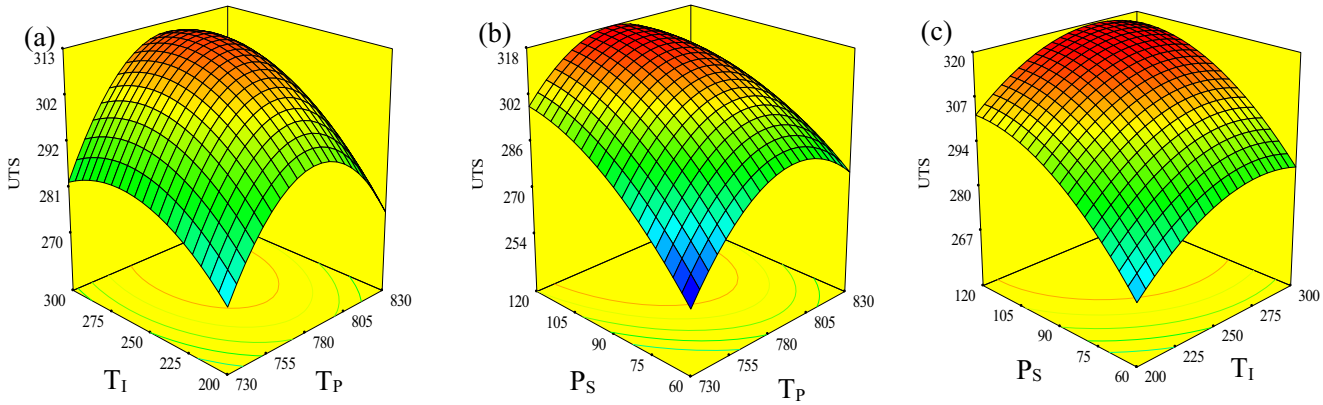

Fig. 6 Response surface graph showing the effects of **a** T_P and T_I, **b** T_P and P_S, and **c** T_I and P_S on UTS

experimental cost. For experimental designs and analyses, various statistical and mathematical techniques have been used by researchers. The purpose of these techniques is to optimize the input variables in order to achieve the desired response value. Techniques which were generally employed for the analysis and optimization include Taguchi method [41], factorial design [42], central composite design [43], Box-Bhenken design [2], genetic algorithm [44], artificial neural network [45], and Fuzzy logic [46]. Among these techniques, Fuzzy logic, genetic algorithm, and artificial neural network are considered as soft computing techniques while factorial design, Taguchi method, central composite design, and Box-Bhenken design are termed as statistical techniques. However, among the statistical techniques, response surface methodology (RSM) is regarded as the best suitable cost-effective technique for the analysis and prediction of response measures. It is a combination of mathematical and statistical techniques normally used for the modeling and optimization of response variables [47, 48]. Keeping in view the number of parameters and their levels, Box-Bhenken design (BBD) of RSM has been found suitable for experimentation [49].

In this experimental methodology, the relationship of response variables with input parameters can be expressed as follows:

$$S = f(T_P, T_I, P_S) \tag{1}$$

where S is the response variable, T_p is pouring temperature, T_I is the insert preheating temperature, and P_S is squeeze pressure. Quadratic model can also be formulated that holds a high prediction accuracy because of its capability to determine the interaction effects of parameters on response variables. Selected regression model can be expressed as follows:

$$S = a_o + \sum_{i=1}^{n} a_i B_i + \sum_{i=1}^{n} a_{ii} B_i^2 + \sum_{i<j}^{n} a_{ij} B_i B_j + \varepsilon \tag{2}$$

Here a_o, a_i, a_{ij}, and a_{ii} are the coefficient of constant linear, interaction, and quadratic terms respectively. While defining the experimental design, 12 factorial and 5 center points were used. In this way, a total of seventeen experiments were performed. Design matrix with experimental results is given in Table 3. Upon successful completion of the experimentation, the prepared samples were subjected to UTS and hardness measurement. UTS was measured on the material testing system (MTS) having a capacity of 100 KN, at room temperature and at a strain rate of 5×10^{-3} mm/s. Hardness of samples was measured using ASTM E384-11 standard on micro Vickers hardness tester (HV-1000). Hardness of samples was measured at five different places on the joint interface area, and their mean value was considered for analysis.

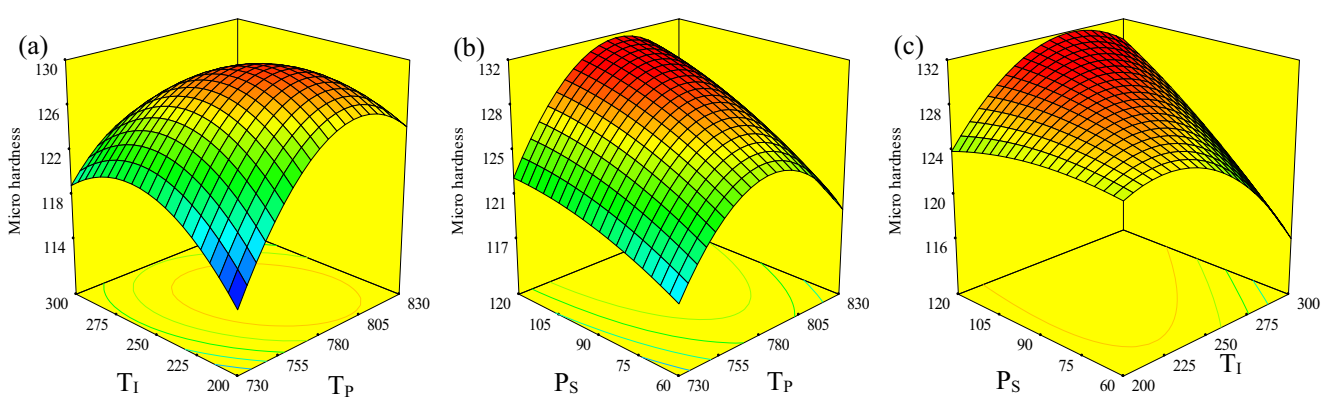

Fig. 7 Response surface graph showing the effects of **a** T_P and T_I, **b** T_P and P_S, and **c** T_I and P_S on MH

Table 4 ANOVA for UTS

Source	SS	df	MS	*F* value	*p* value	
Model	5549.8	9	616.6	89.71	< 0.0001	Significant
T_P	183.4	1	183.4	26.68	0.0013	
T_I	559.5	1	559.5	81.39	< 0.0001	
P_S	2073.7	1	2073.7	301.69	< 0.0001	
$T_P \times T_I$	28.1	1	28.1	4.09	0.0829	
$T_P \times P_S$	128.8	1	128.8	18.74	0.0034	
$T_I \times P_S$	3.8	1	3.8	0.55	0.4812	
T_P^2	1741.1	1	1741.1	253.30	< 0.0001	
T_I^2	317.6	1	317.6	46.21	0.0003	
P_S^2	301.4	1	301.4	43.84	0.0003	
Residual	48.1	7	6.9			
Lack of fit	39.8	3	13.3	6.35	0.0531	Not significant
Pure error	8.3	4	2.1			
Cor total	5597.9	16				
Std. Dev.	2.62		R^2		0.991	
Mean	292.7		Adj R^2		0.980	
C.V. %	0.90		Pred R^2		0.884	
PRESS	649.3		Adeq precision		30.68	

3 Results and discussion

Experimental results have been thoroughly evaluated through various statistical analyses: parametric main effects plots, interaction effects, and analysis of variance. Moreover, scanning electron microscopic and EDX analyses have also been employed to investigate the microstructural features. Empirical modeling, validation of proposed models, and multi-objective optimization have also been carried out. The details of which are discussed in the forthcoming sections.

Table 5 ANOVA for micro-hardness

Source	SS	df	MS	*F* value	*p* value	
Model	483.78	9	53.75	164.38	< 0.0001	Significant
T_P	27.75	1	27.75	84.86	< 0.0001	
T_I	4.95	1	4.95	15.12	0.0060	
P_S	81.73	1	81.73	249.92	< 0.0001	
$T_P \times T_I$	37.76	1	37.76	115.47	< 0.0001	
$T_P \times P_S$	3.86	1	3.86	11.81	0.0109	
$T_I \times P_S$	58.52	1	58.52	178.96	< 0.0001	
T_P^2	167.06	1	167.06	510.87	< 0.0001	
T_I^2	79.36	1	79.36	242.69	< 0.0001	
P_S^2	3.73	1	3.73	11.41	0.0118	
Residual	2.29	7	0.33			
Lack of fit	1.49	3	0.50	2.51	0.1976	Not significant
Pure error	0.79	4	0.20			
Cor total	486.07	16				
Std. Dev.	0.57		R^2		0.995	
Mean	123.7		Adj R^2		0.989	
C.V. %	0.46		Pred R^2		0.948	
PRESS	25.16		Adeq precision		35.891	

Table 6 Summary of main, interaction, and quadratic factors influencing UTS and MH

Factors	UTS (MPa)	MH (HV)
T_P	✓	✓
T_I	✓	✓
P_S	✓	✓
$T_P \times T_I$		✓
$T_P \times P_S$	✓	✓
$T_I \times P_S$		✓
T_P^2	✓	✓
T_I^2	✓	✓
P_S^2	✓	✓

3.1 Parametric main effects plots

To examine the trend of input parameters with respect to the selected responses (UTS and MH), main effects plots have been drawn and presented in Figs. 4 and 5. It can be seen from Fig. 4 that UTS enhanced with an increase in T_P up to a pouring temperature of 780 °C whereas a further increase in T_P yields lower UTS value. This happens because at lower T_P, metallurgical bonding between solid insert and casting material is weaker due to a decreased diffusion coefficient. On the other end, if pouring is done at a higher T_P, it causes the severe melting of the insert. Eventually, poor metallurgical bonding

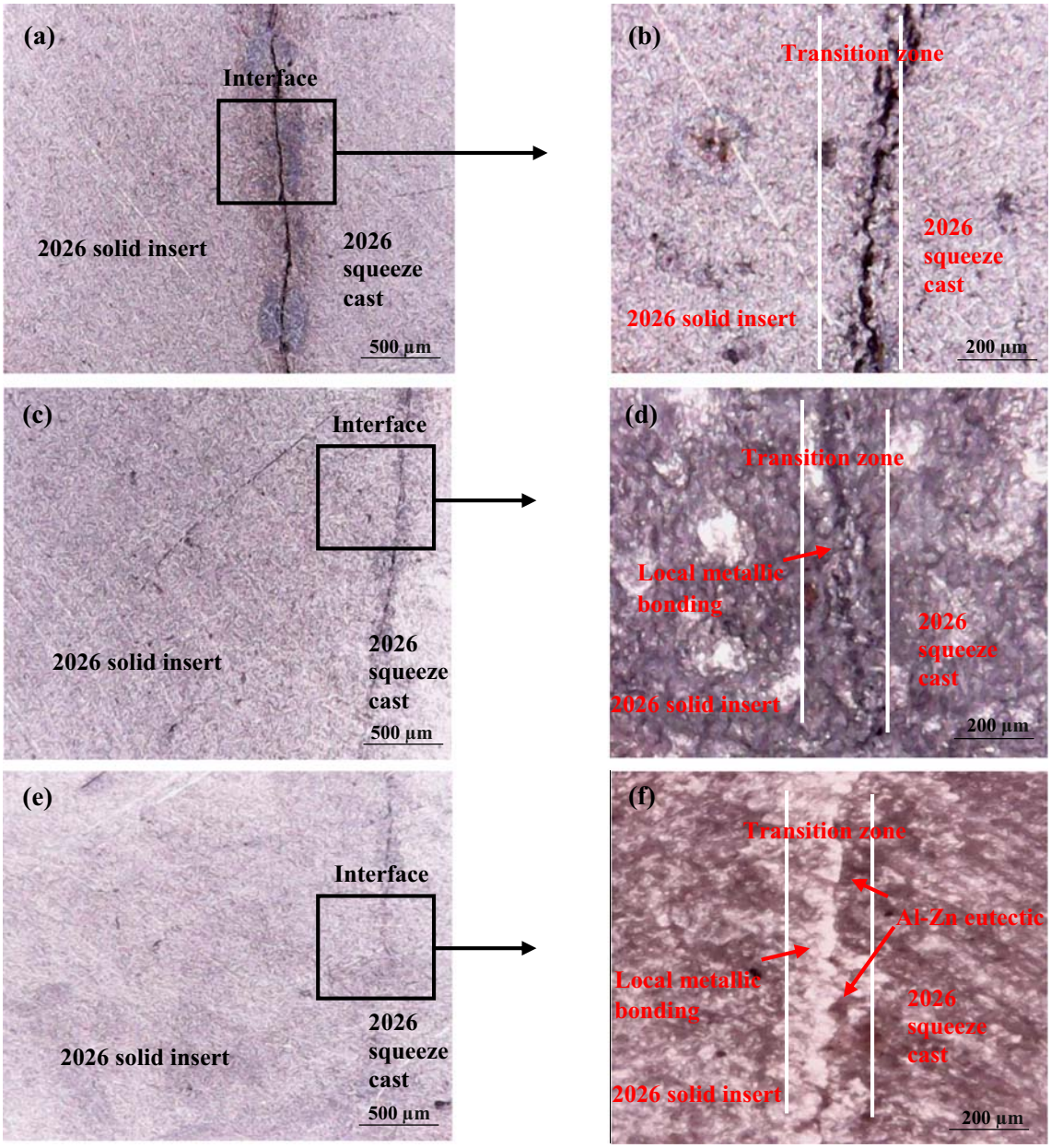

Fig. 8 Microstructure images of the interface of 2026-2026 aged overcast joints made at different conditions. **a**, **b** 730 °C T_P, 250 °C T_I, and 60 MPa P_S. **c**, **d** 830 °C T_P, 200 °C T_I, and 90 MPa P_S. **e**, **f** 780 °C T_P, 300 °C T_I, and 120 MPa P_S

is observed that results in a lower value of UTS [31]. It has also been inferred that UTS increases with increment in T_I. The value of UTS comes out to be minimum at a low level of T_I (200 °C) whereas the maximum value of UTS is achieved at mid-level of T_I.

This is attributed to the weak metallurgical bonding that was observed at lower T_I. Actually at lower T_I, poor diffusion occurs between the melt and solid insert. The quality of bond developed in this regard is inferior due to poor diffusion which causes lower UTS value. Contrarily, a further rise in T_I from 250 to 300 °C provides a lower magnitude of UTS. This reduction in UTS is linked with complete removal of the coating layer of the zinc from the insert surface at a higher value of T_I. When a high-temperature melt is poured into the die, the heat flux is transferred to the solid insert which is already placed into the die. This temperature rise tends to peel off the coating layer of zinc from the insert. The chance of removal of this coating layer during the melt pouring process upsurges if insert already holds a high temperature. Because of both the said arguments, the zinc coating layer might have been removed and thus week bonding has been developed between the insert and the melt. This has also been witnessed from the UTS value observed at the larger magnitude of T_I. The magnitude of UTS has also depicted an improvement with the rise in P_S. Maximum UTS was obtained at a higher level of P_S (120 MPa), because the application of high pressure on the molten material minimizes the possibility of gas entrapment, hot tears, and shrinkage cavities in the casting [50]. Reduction in the aforesaid casting defects resulted in an improvement in the UTS values.

The effects of input parameters (T_P, T_I, and P_S) on MH are described in Fig. 5. It has been observed that MH has a nonlinear trend with respect to all the control parameters, i.e., T_P, T_I, and P_S. The magnitude of MH is noted to be maximum at a middle level of T_p (780 °C) because an appropriate diffusion might have occurred between the insert and the melt. It has already been reported that MH has a direct dependence on the diffusion of melt and solid insert. If the poor diffusion of melt and solid insert occurs, it will yield inferior metallic bonding that reduces the value of MH [9, 32]. Thus, the higher magnitude of MH is a proof of better diffusion of melt and the solid insert. Any increase or decrease in T_P beyond 780 °C is found to have a negative impact on the micro-hardness of the joint. Similar trend has also been demonstrated by T_I for MH. Middle level of T_I provides better MH at the joint interface. Lower T_I generates an insufficient diffusion of melt and solid insert. Subsequently, a weaker bond is formed that depicts smaller MH. While at high T_I, possibly the zinc coating has vanished from the insert surface as the melt is poured. Due to a lack of zinc coating, improper metallic bonding between solid insert and melt occurs which results in a reduction of MH. Another important finding observed from Fig. 5 is that the highest MH can be achieved at P_S of 120 MPa. It is due to the fact that at low P_S premature solidification occurs which propagates nucleation and micro cracks which in turn reduce the hardness of joint interface [4, 19].

3.2 Interaction effects analysis

To have a distinct understanding of the effect interactions on the responses, 3D response surface plots have been drawn and analyzed. The 3D response plots can simultaneously analyze the effect of two parameters on the selected response while keeping all the other parameters at the middle level. The study of interaction effects of parameters which cannot be studied by other types of response graphs is the major advantage of 3D surface graphs. The 3D surface plots for both UTS and MH are represented in Figs. 6 and 7.

Figure 6a shows the combined effect of T_P and T_I on UTS simultaneously. It has been observed that UTS is minimum (271 MPa) at T_P of 730 °C and T_I of 200 °C. However, the maximum (312.7 MPa) UTS was achieved at T_I equal to 283 °C and T_P equal to 794 °C. Furthermore, it has been revealed that T_P has a larger impact on UTS as compared with T_I. Figure 6b depicts the collective impact of P_S and T_P on UTS at once. It has been detected that the lower value of UTS

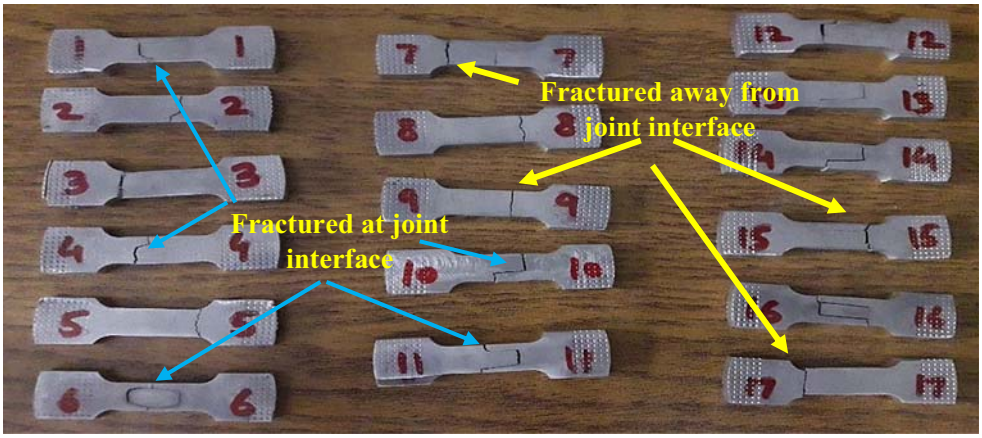

Fig. 9 Fractured samples after UTS testing

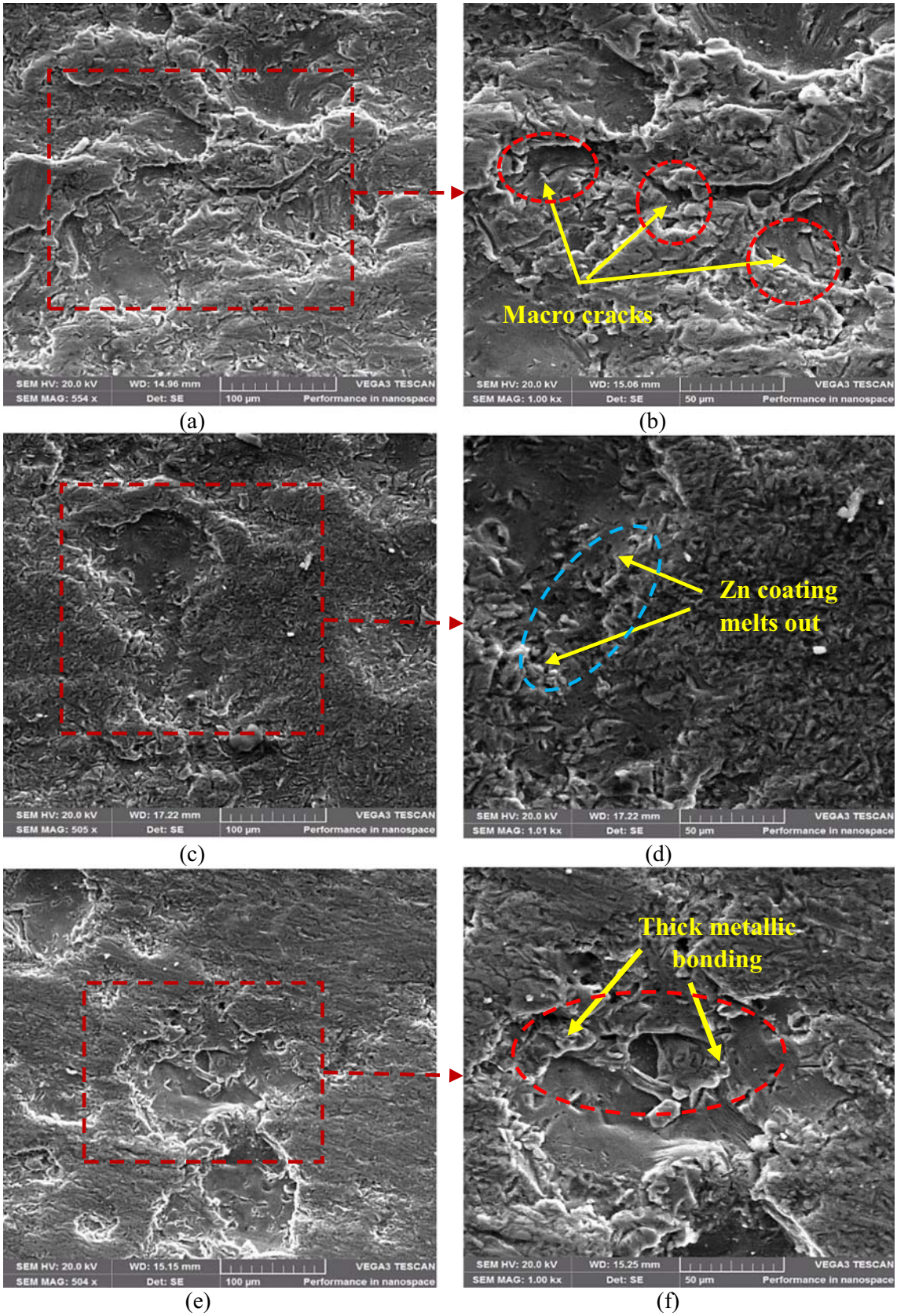

Fig. 10 SEM image of the flat surface of samples 7, 8, and 3 made at different input parameters. **a**, **b** 730 °C T_P, 250 °C T_I, and 60 MPa P_S. **c**, **d** 830 °C T_P, 200 °C T_I, and 90 MPa P_S. **e**, **f** 780 °C T_P, 300 °C T_I, and 120 MPa P_S

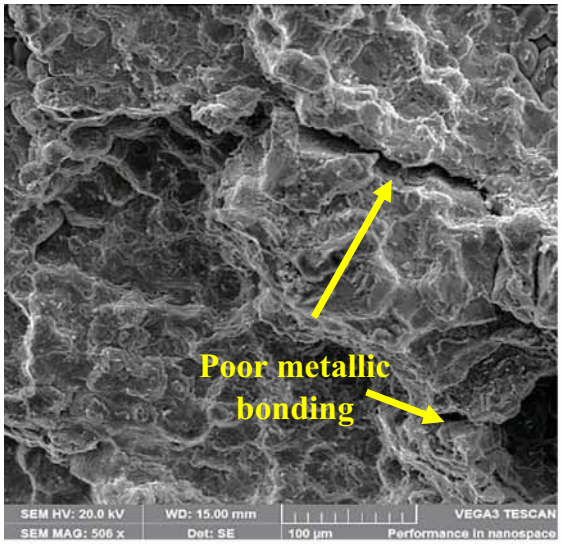
Poor metallic bonding
SEM HV: 20.0 kV
WD: 15.00 mm
VEGA3 TESCAN
SEM MAG: 506 x
Det: SE
100 μm
Performance in nanospace

(a)

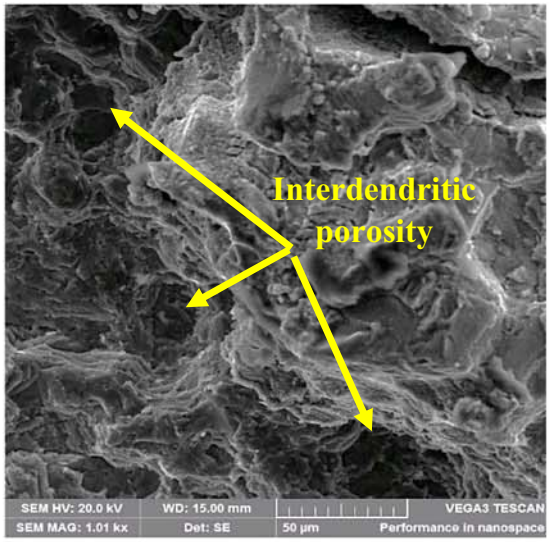
Interdendritic porosity
SEM HV: 20.0 kV
WD: 15.00 mm
VEGA3 TESCAN
SEM MAG: 1.01 kx
Det: SE
50 μm
Performance in nanospace

(b)

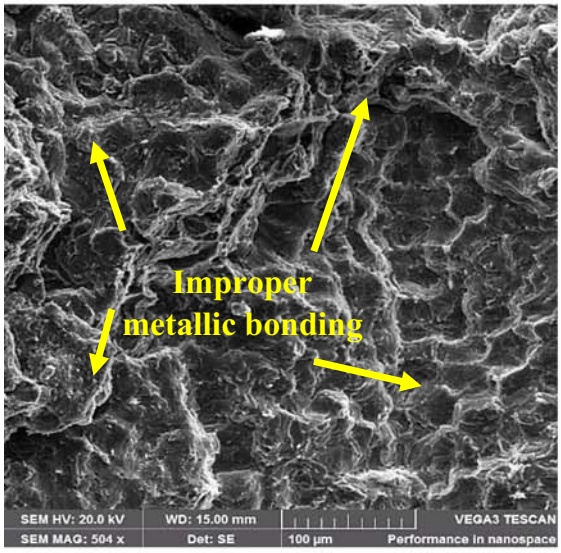
Improper metallic bonding
SEM HV: 20.0 kV
WD: 15.00 mm
VEGA3 TESCAN
SEM MAG: 504 x
Det: SE
100 μm
Performance in nanospace

(c)

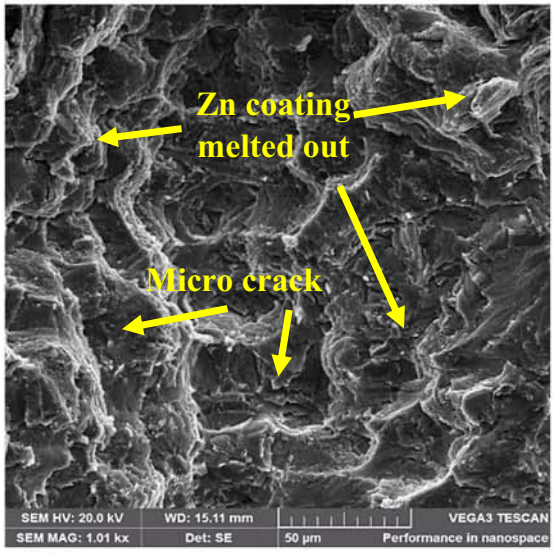
Zn coating melted out
Micro crack
SEM HV: 20.0 kV
WD: 15.11 mm
VEGA3 TESCAN
SEM MAG: 1.01 kx
Det: SE
50 μm
Performance in nanospace

(d)

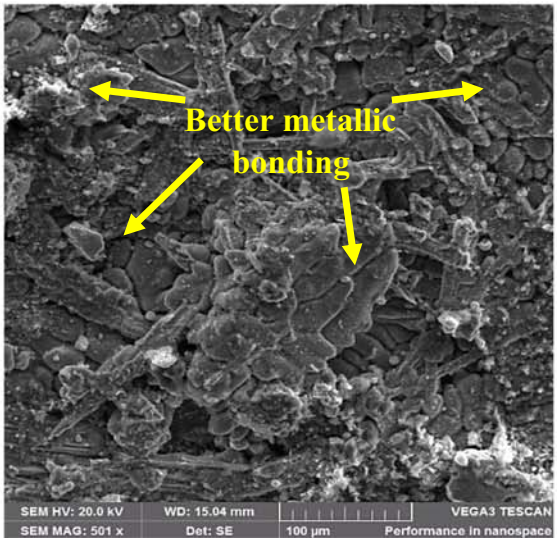
Better metallic bonding
SEM HV: 20.0 kV
WD: 15.04 mm
VEGA3 TESCAN
SEM MAG: 501 x
Det: SE
100 μm
Performance in nanospace

(e)

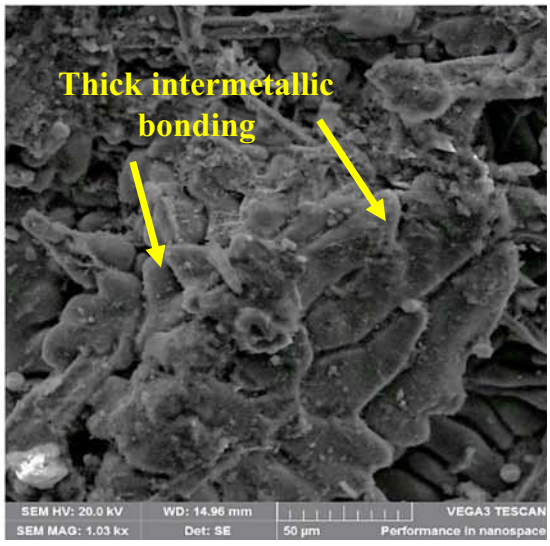
Thick intermetallic bonding
SEM HV: 20.0 kV
WD: 14.96 mm
VEGA3 TESCAN
SEM MAG: 1.03 kx
Det: SE
50 μm
Performance in nanospace

(f)

◀ **Fig. 11** SEM image of the fracture surface of samples 7, 8, and 3 made at different input parameters. **a**, **b** 730 °C T_P, 250 °C T_I, and 60 MPa P_S. **c**, **d** 830 °C T_P, 200 °C T_I, and 90 MPa P_S. **e**, **f** 780 °C T_P, 300 °C T_I, and 120 MPa P_S

(255 MPa) was obtained at P_S of 60 MPa and T_P of 730 °C. On the other end, the largest value of UTS (318 MPa) was attained at a squeeze pressure of 116 MPa and at a pouring temperature of 784 °C. It can be observed that UTS has been greatly affected by P_s in comparison with T_p. The combined effects of P_S and T_I on UTS were mentioned in Fig. 6c. This graph demonstrates that UTS was minimum (268 MPa) when the values of P_S and T_I were at their lower levels. Opposite to that, higher (319.5 MPa) UTS has been achieved at P_S of 114 MPa and T_I of 267 °C. Moreover, the influence of P_S on UTS was found more dominant in contrast to T_I.

The interaction effects on control parameters for MH were portrayed in Fig. 7. The combined effect of T_P and T_I on micro-hardness (MH) simultaneously has been illustrated by Fig. 7a. It has been perceived that MH was minimum (114.3 HV) at a T_P of 730 °C and at a T_I of 200 °C. The maximum (129.3 HV) of MH was recorded when T_I was set at 245 °C and T_P was equals to 790 °C. It has also been observed that T_P has a larger influence on MH as compared with T_I. Figure 7b describes the combined impact of P_S and T_P on MH. It has been discerned that the lower value of MH (117.8 HV) was obtained at 60 MPa P_S and 730 °C T_P. Contrary to that, larger value of MH (131.6 HV) was achieved at 110 MPa P_S and 790 °C T_p. Moreover, it has been envisaged from the 3D plot mentioned in Fig. 7b that T_P is more influential for MH as compared with P_S. The combined effects of P_S and T_I on MH were shown in Fig. 7c. The plot revealed that greater (131 HV) MH was materialized at 114 MPa of P_S and 246 °C of T_I. The impact of P_S on MH was also found slightly more significant than that of T_I.

3.3 Analysis of variance

ANOVA has been performed after thoroughly discussing the parametric and interaction effects to evaluate their significance towards the selected responses. Statistical significance of process parameters, interaction, and quadratic terms has been gauged at a confidence interval of 95%. Results of ANOVA are tabulated in Tables 4 and 5. According to the said defined criterion of 95%, any of the control variables having a p value lower than 0.05 would be rated as significant for the selected response. It has been revealed that all the input parameters are significant for UTS as their p values are less than 0.05 as mentioned in Table 4. It is important to mention all the quadratic terms are significantly affecting UTS, but in the case of interactions, only one interaction term ($T_P \times P_S$) has been found significant for UTS. In Table 5, the ANOVA results for MH were introduced. It has been revealed that pouring temperature, insert preheating temperature, and squeeze pressure are the significant input parameters for MH. The p value of all the parameters was lower than the set alpha value of 0.05. In addition to the input parameters, all the interactions and quadratic terms are also observed significant for the MH. It is pertinent to mention that the model developed for MH is statistically significant as its p value (0.0001) is far less than the alpha value.

The above discussion explains the main, interaction, and quadratic effects of input parameters (T_P, T_I, and P_S) on the responses (UTS and MH). These input parameters must be carefully controlled to attain optimum results. The summary of the main, interaction, and quadratic factors influencing UTS and MH are presented in Table 6. It is evident from Table 6 that the main factors T_P, T_I, and P_S and quadratic terms are significantly influencing both the responses. However, only one interaction term ($T_P \times P_S$) has proved significant for UTS. But in the case of MH, all the interaction terms are rated as significant.

Microstructures of the interface of 2026-2026 aged overcast joints were made at different conditions as shown in Fig. 8a–f. When the pouring temperature and insert preheating were low, poor melting of Zn coating occurred which causes the inadequate wettability between solid insert and 2026 squeeze casted material. This poor bonding was evidenced in optical micrographs shown in Fig. 8a, b. On the other end, at high temperature, severely undesired melting of Zn coating occurs that results in less strong local metallic bonding as highlighted in Fig. 8c, d. It has been observed that complete local metallic boning obtained among the 2026 Al solid insert and 2026 squeeze casted material at 780 °C T_P, 300 °C T_I, and 120 MPa P_S as evidenced in Fig. 8e, f. The formation of this complete bonding is attributed to the appropriate melting of the Zn coating. Such an apt melting of the coated layer facilitates the appreciable diffusion of the insert material to the melt. Thus, a strong intermetallic bond is achieved between the solid insert and squeeze casted material. It is worthy to note that the strength of intermetallic bonding in case of overcasting is not only dependent on the physical properties of the material of melt, solid insert, and interface temperature [51], rather Zn coating also holds a pivotal role in governing the strength of bonding as evidenced in this research. Furthermore, the quality of the interface bond also seemed to have a close relationship with the squeeze pressure. A low value of squeeze pressure yields a poor intermetallic bonding between solid insert and squeeze casted material. The low squeeze pressure has also been cited as a source of inherent defects formation in the casted parts [31]. Contrarily, at a high squeeze pressure, a strong and compact intermettalic bonding is achieved with minimum defects as shown in Fig. 8e–f. The mechanical properties of such castings obtained at high

squeeze pressure are notably better in contrast to that achieved at low squeeze pressure as depicted in Fig. 8a, b, c, d.

3.4 Scanning electron microscopic analysis

In addition to comprehensively discussing the effects of control parameters on the responses, microstructural characterization of a flat and fractured surface of samples has been carried out with a scanning electron microscope (SEM: VEGA3). Fractured samples after UTS testing have been shown in Fig. 9. Some of the samples were broken at the joint interface while others were broken away from the joint interface which depicts that the overcast joint has more strength than the casted material. SEM images of a flat surface and fractured surface of samples obtained under different experimental conditions are shown in Figs. 10a–f and 11a–f. Two magnification ranges (× 500 and × 1000) have been selected for fractography. SEM images in Figs. 10a, c, e and 11a, c, e have

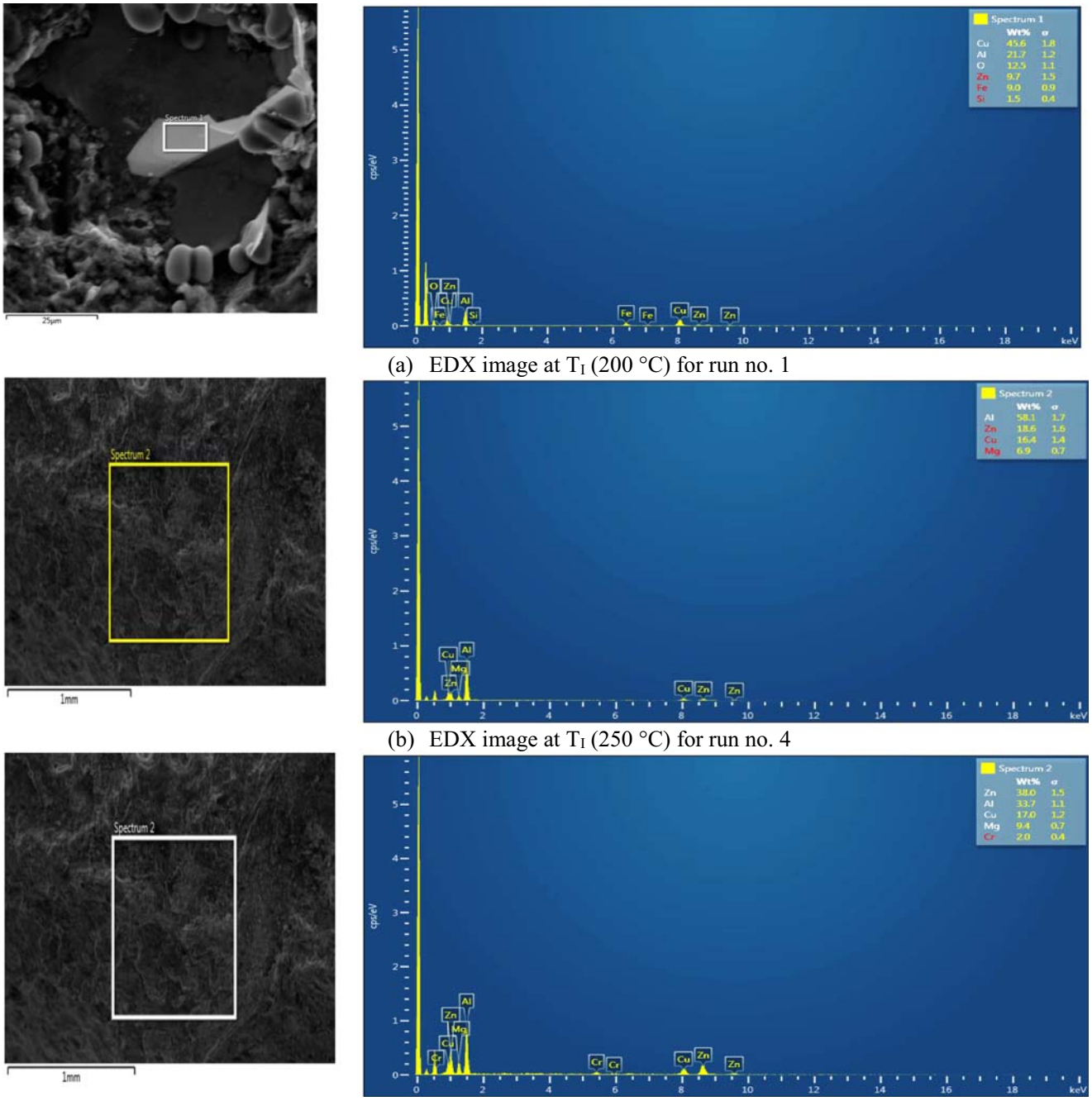

(a) EDX image at T_I (200 °C) for run no. 1

(b) EDX image at T_I (250 °C) for run no. 4

(c) EDX image at T_I (300 °C) for run no. 6

Fig. 12 EDX images of samples at three levels of T_I (**a**–**c**). **a** EDX image at T_I of 200 °C for run no. 1. **b** EDX image at T_I of 250 °C for run no. 4. **c** EDX image at T_I of 300 °C for run no. 6

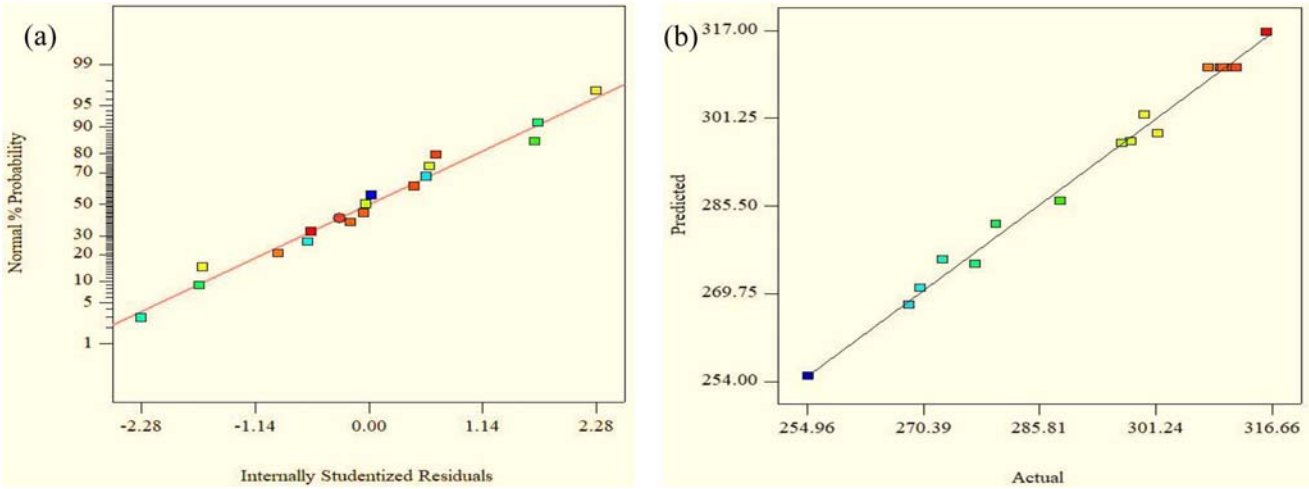

Fig. 13 Normal plot of residuals for UTS (**a**) and predicted vs. actual plot for UTS (**b**)

been taken at × 500 magnification, whereas Figs. 10b, d, f and 11b, d, f are at × 1000.

Figure 10a and b show the flat surface of sample no. 7. Macro cracks in SEM images have been observed because of low squeeze pressure (60 MPa). This inherent defect is the primary cause of low UTS and MH. Figure 10c and d represent the SEM micrograph of sample no. 8. It has been examined in SEM images that Zn coating completely melts out at high pouring temperature (830 °C). Thus, poor intermetallic bonding between Al melt and solid insert occurred. Figure 10e and f illustrates the flat surface of samples no. 3. Macro cracks and shrinkage cavities were removed due to high squeeze pressure and Zn coating at solid insert had made the thick intermetallic bonding with melt due to controlled pouring temperature.

In addition to SEM analysis of as-casted samples, fractography of fractured samples has also been done to envisage the type of fracture as highlighted in Fig. 11, which shows the fractographic images of sample no. 7. During trial no. 7, the values of UTS and MH were found minimum, i.e., 255 MPa and 118.2 HV, respectively and their microstructure was shown in Fig. 11a, b. There, brittle fracture having cluster-like morphology was observed. Because at low squeeze pressure and pouring temperature, poor metallic bonding occurs between solid insert and pouring material. The poor metallic bonding is attributed to the interdendritic porosity and improper melting of Zn coating into Al melt that yields inherent defects [26].

Figure 11c and d represents the fracture structure of sample no. 8 which provided an approximately average value of UTS (277.3 MPa) and MH (124.6 HV), respectively. Once again brittle-type fracture has been noted but having comparably a flatter morphology. This flatness is predominantly owing to the rise in squeeze pressure. As in experiment 8, the value of P_S was 90 MPa which is lightly higher to 60 MPa obtained for the case of the 7th experimental run. It has already been testified that the increase in P_S tends to reduce the macro cracks and subsequently falter morphology. Though in the 8th

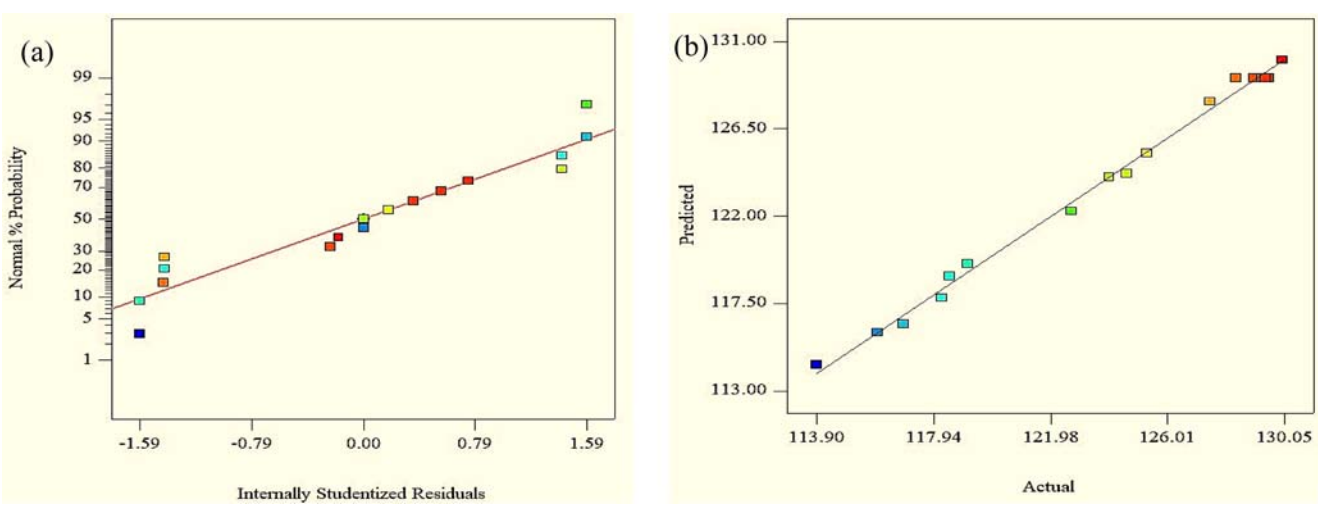

Fig. 14 Normal plot of residuals for MH (**a**) and predicted vs. actual plot for MH (**b**)

Table 7 Confirmatory experiments for UTS and MH with predicted and actual values

SR. No.	Process parameters				Response results	
	Pouring temperature (°C)	Insert temperature (°C)	Squeeze pressure (MPa)		UTS (MPa)	Micro-hardness (HV)
1	760	230	70	Actual	280.90	120.20
				Predicted	284.50	125.20
				% error	1.27	3.75
2	800	270	110	Actual	313.30	128.00
				Predicted	316.56	130.30
				% error	1.03	1.77
3	800	230	70	Actual	294.20	122.80
				Predicted	290.00	127.20
				% error	1.45	3.44
4	760	270	110	Actual	309.50	125.70
				Predicted	314.90	129.30
				% error	1.71	2.78
5	800	230	70	Actual	294.00	129.00
				Predicted	290.60	127.20
				% error	1.17	1.44
6	760	270	110	Actual	310.00	131.00
				Predicted	314.90	129.30
				% error	1.56	1.31
7	760	230	70	Actual	280.00	120.10
				Predicted	284.00	125.00
				% error	1.41	3.92
8	800	270	110	Actual	312.72	128.54
				Predicted	316.56	130.33
				% error	1.21	1.37

experimental trial, the greater value of P_S improves the bonding but still the strength of the bond is compromised because of high pouring temperature, i.e., 830 °C. This high pouring temperature causes severe melting of Zn coating from the solid insert and therefore improper metallic binding has been noticed [10, 32]. Figure 10e and f represents the fracture structure of sample no. 3. The values of UTS and MH have been noted as maximum, i.e., 315.9 MPa and 130 HV, respectively.

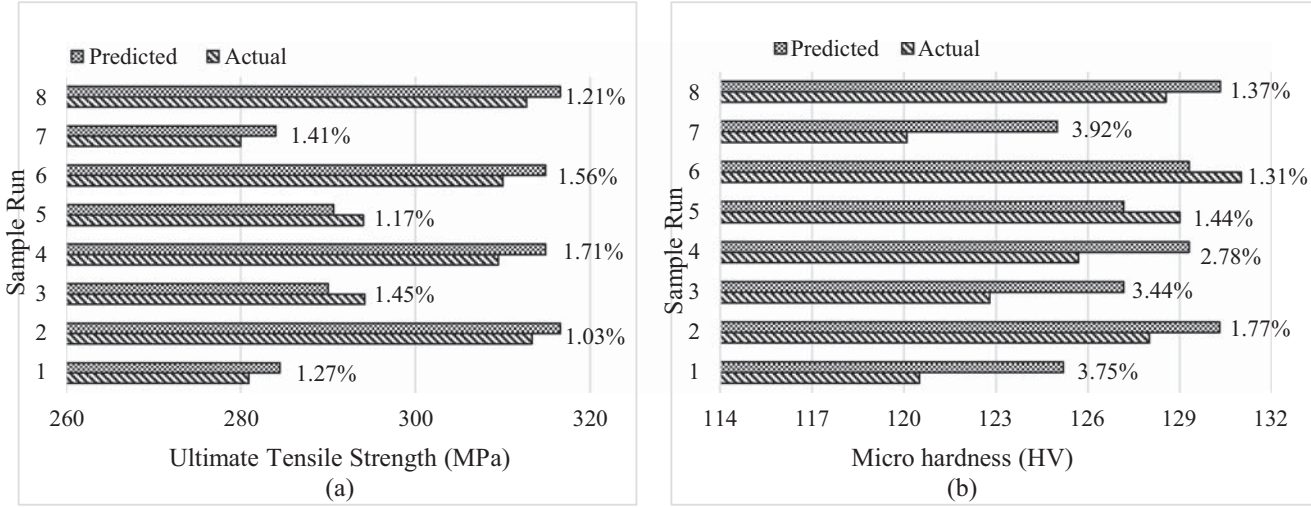

Fig. 15 Percentage error % between actual and predicted UTS (**a**) and micro-hardness (**b**)

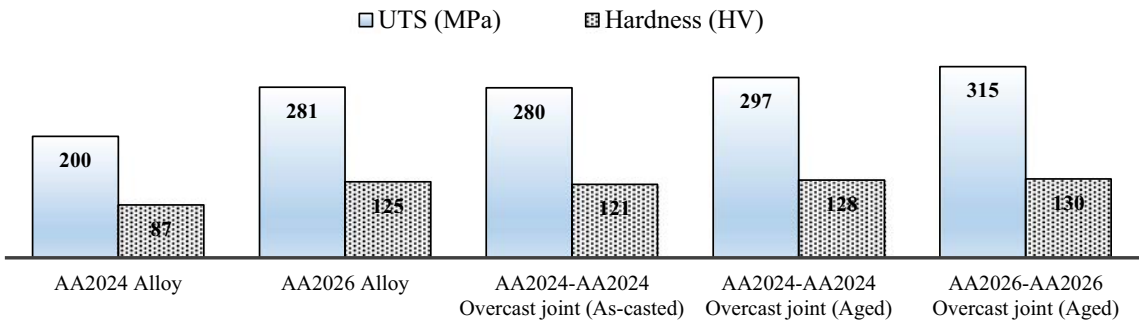

Fig. 16 Comparison of AA2026-AA2026 overcast joint (aged) with base metal A2026 alloy, A2024 alloy, AA2024-AA2024 overcast joint (as-casted and aged)

Furthermore, brittle fracture has been revealed with more flatter-face morphology. The depiction of such morphology is an indication of thick metallic bonding between solid insert and Al melt [10]. The same has also been witnessed in the SEM images described in Fig. 11e, f. The formation of this thick metallic bonding is due to the high squeeze pressure (120 MPa). It has cited in another work conducted in the same field that increment in squeeze pressure reduces the inherent defects like macro cracks and shrinkage cavities [28, 29]. So, the current finding is validated by the already existing literature in the field. Insert temperature, whose effect on UTS and MH has not been explored yet, shows a significant impact of both the selected responses. Higher value of insert temperature results in better UTS and MH as it ensures an appropriate bond formation between the melt and the insert. The thick metallic boding at a larger T_I is also evidenced in SEM micrographs provided in Fig. 11e, f.

3.5 EDX analysis

Samples have been examined using EDX to evaluate the impact of the insert preheating on the aged A2026-A2026 overcast joints. EDX images (Fig. 12) have been taken for three different samples (run number 1, 4, 6). Figure 12a demonstrates that at low T_I (200 °C) poor melting of Zn coating (9.7 wt%) from solid insert was the main reason of weak intermetallic bonding between solid insert and squeeze casted, while the sample's UTS and MH were 270 MPa and 113.9 HV, respectively. From Fig. 12b, a strong intermetallic bonding among the solid insert material and squeeze casted material which was due to proper melting of Zn coating (18.6 wt%) from solid insert during pouring of melt has been observed at T_I (250 °C), while the sample has higher UTS (310.2 MPa) and MH (129.4 HV), respectively. Figure 12c depicts the weak bonding of solid insert and squeeze casted material due to the severe melting of Zn coating (38 wt%), while the sample has lower UTS (297.9 MPa) and MH (116.9 HV) compared with run no. 4.

3.6 Empirical modeling

Another important aspect of the present research was the formulation of mathematical models of input variables with respect to responses that has not been explicitly targeted yet. Based on the RSM experimental methodology, empirical relations of control variables with UTS and MH are presented in Eqs. 3 and 4. For both the responses, nonlinear quadratic model has noted suitable as the value of its Adj. R^2 comes out to be more than 98% for UTS as well as MH. The statistical significance of the proposed relations has also been validated through ANOVA as highlighted in Tables 4 and 5. p value of both the mathematical models has observed far less than the defined alpha value that proofs the statistical significance of the formulated models.

$$\begin{aligned} \mathrm{UTS} = {} & -5169.98 + 12.86 \times T_P + 1.14 \times T_I + 5.34 \\ & \times P_S + 0.00106 \times T_P \times T_I – 0.00378 \times T_P \\ & \times P_S – 0.00065 \times T_I \times P_S – 0.00813 \\ & \times T_P^2 – 0.00347 \times T_I^2 – 0.0094 \times P_S^2 \end{aligned} \quad (3)$$

Table 8 Comparison of % improvement in UTS and hardness of AA2026-AA2026 with 2000 series alloys

Comparison		UTS	Hardness
AA2026-AA2026 overcast joint (aged)	AA2024 alloy [18]	57.50%	49.42%
	AA2026 alloy (squeeze casted) [42]	12.09%	4.0%
	AA2024-AA2024 (as-casted) [18]	12.50%	7.43%
	AA2024-AA2024 (aged) [18]	5.70%	1.53%

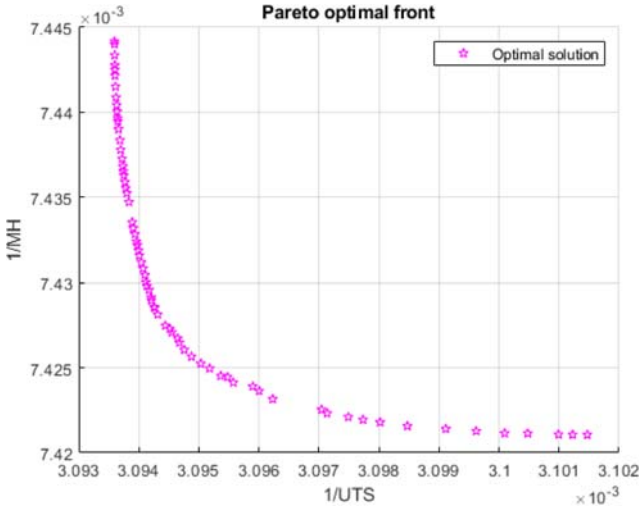

Fig. 17 Pareto fronts of MO-GA

$$\mathrm{MH} = -1691.84 + 4.21 \times T_{\mathrm{P}} + 1.58 \times T_{\mathrm{I}} - 0.853 \times P_{\mathrm{S}} - 0.00122 \times T_{\mathrm{P}} \times T_{\mathrm{I}} + 0.00065 \times T_{\mathrm{P}} \times P_{\mathrm{S}} + 0.00255 \times T_{\mathrm{I}} \times P_{\mathrm{S}} - 0.00251 \times T_{\mathrm{P}}^2 - 0.00173 \times T_{\mathrm{I}}^2 - 0.00104 \times P_{\mathrm{S}}^2 \quad (4)$$

Validation of the proposed models has also been examined via a normal probability plot of residuals and predicted versus actual values. These plots are presented in Figs. 13 and 14. The normal plot of residuals for UTS is shown in Fig. 13a, most of the data points lie on the line that depicts the normal distribution of the error. Moreover, predicted vs. actual plot illustrates that points lie closer to the fitted line which means predicted values are in good agreement with the actual values as shown in Fig. 13b.

Figure 14a represents the normal probability plot of the residuals for MH. Mostly point lies reasonably closer to the trend line which indicates the normal distribution of error. Figure 14b demonstrates the graph of predicted vs. actual values of MH. In the graph, the data points lie near the fitted line which is an indication that actual data is very close to predicted data. The models' prediction adequacy has also been witnessed through the aforementioned statistical tests.

3.7 Validation of proposed empirical models

The validation of the developed empirical models for UTS and MH has also been tested by conducting eight confirmatory experiments. For these experiments, random values of input parameters have been chosen within the design space (other than that used for the development of empirical models). The results obtained from the confirmatory experiments are described in Table 7. To calculate the percentage error between the actual and predicted values of UTS and MH, Eq. (5) has been used [19]. The results of percentage error are mentioned in Fig. 15. It has been noticed that percentage error for all the eight confirmatory trials is less than 5%, which depicts the validity of developed models for UTS and MH.

$$\text{Percentage error} = \left| \frac{\text{actual value} - \text{predicted value}}{\text{predicted value}} \right| \times 100 \quad (5)$$

The prominence of squeeze overcasting can be perceived by comparing maximum UTS and MH attained through squeeze overcasting (aged AA2026-AA2026 overcast joint) with the resultant values of base metal AA2026 alloy, AA2024 alloy, and AA2024-AA2024 overcast joint (as-casted and aged) [19, 47] as shown in Fig. 16. It is evident from Fig. 16 that the improvement in UTS and MH is highest for AA2026-AA2026 overcast joint than that of others. This significant enhancement in UTS and MH clearly vindicates the effectiveness of aged squeeze overcasting. The improvement percentage of UTS and hardness of AA2026-AA2026 for 2000 series alloys and overcast joints have been given in Table 8. UTS of AA2026-AA2026 overcast joint (aged) has been increased by 12% as compared with UTS of AA2026 squeeze casted alloy. Moreover, the magnitude of MH was also improved by 4%.

Table 9 Confirmation tests for optimal values

Methodology	Evaluation criteria		Input parameters			Response indicators					
			Pouring temperature (T_P)	Insert preheating (T_I)	Squeeze pressure (P_s)	Ultimate tensile strength (UTS)			Micro-hardness (MH)		
						Pred.	Act.	% Dev.	Pred.	Act.	% Dev.
RSM	Single objective	Max UTS	784	267	114	322.9	316.2	2.11	133.9	127.7	4.85
		Max MH	790	246	110	319.4	313.6	1.84	133.5	128.2	4.13
MO-GA	Multi-objective	Max UTS, Max MH	781	272	117	323.2	320.1	0.96	134.7	132.9	1.35

RSM, response surface methodology; *MO-GA*, multi-objective optimization genetic algorithm

3.8 Multi-objective optimization

The RSM-based empirical models of micro-hardness and ultimate tensile strength have been used as objective functions for optimization using multi-objective genetic algorithm (MO-GA). MATLAB 2019a software package is utilized for the execution of MO-GA. The objective was to maximize both responses within following continuous parameters subject to the following:

$$730 \le T_p \le 830$$

$$200 \le T_i \le 300$$

$$60 \le P_s \le 120$$

$$\text{Objective}_1 = \text{Minimize}\left(\frac{1}{\text{UTS}}\right)$$

$$\text{Objective}_2 = \text{Minimize}\left(\frac{1}{\text{MH}}\right)$$

The MO-GA parameters considered during the execution are as follows: population of 200, crossover rate of 80%, and mutation rate of 5%. To optimize both of the responses, a number of combinations of crossover and mutation were tried which were found suitable in enhancing the traits of MO-GA. High crossover ensures maintaining optimal fits while low mutation helps in not losing genetic traits while flipping. Pareto optimal front's both responses were shown in Fig. 17.

Overall 75 optimal solutions were obtained, and a confirmation test was conducted for verification purposes of the optimal combination of input parameters. An optimal set of variable factors optimizing both responses was obtained. Furthermore, the most favorable set of input parameters for individual responses taken from interaction plots, generated through RSM, are reported in Table 9. The variability of optimal tests obtained from RSM and MO-GA has been ensured, and the average value was reported along with the deviation from the predicted value in Table 9. The overall average error between predicted and actual tests was found lower than 5% ensuring the confidence in optimal solutions.

4 Conclusion

The objective of this research was to investigate the influences of squeeze casting input parameters (pouring temperature T_P, insert preheat temperature T_I, and squeeze pressure P_S) on the mechanical properties (ultimate tensile strength (UTS) and micro-hardness (MH)) of aged AA2026-AA2026 overcast joints. Response surface methodology with Box-Bhenken design has been used for the experimental design matrix. Experimental results have been analyzed with different statistical tests and SEM analyses. The following conclusions may possibly be drawn for the present research:

- Experimental results revealed that the squeeze overcasting (AA2026-AA2026) could be a valuable alternative for the casting of AA2026 alloy. Supremacy of squeeze overcasting has been verified by comparing it with the mechanical properties (UTS and MH) of squeeze casted A2026 alloy. Maximum values of UTS and MH achieved at an optimal parametric combination (P_S of 120 MPa, T_P of 780 °C, and T_I of 250 °C) during squeeze overcasting are 315 MPa and 130 HV respectively.
- The main effects plot analysis depicts that both T_P and P_S portrayed similar trends for UTS as well as MH. An increase in the T_P up to the middle value (780 °C) resulted into higher magnitude of UTS and MH whereas a further rise in T_P tends to produce weak metallic bonding that was translated into lower UTS and MH. On the other end, higher value of P_S provides a larger value of UTS and MH as at higher P_S the probability of casting defects (cracks and porosities) formation was minimized.
- Interaction effects plots demonstrate that the UTS was highly affected by P_S followed by T_P and T_I. In the case of MH, T_P was the most significant parameter followed by P_S and T_I. It has been observed that maximum UTS was obtained at 784 °C of T_P, 114 MPa of P_S, and 267 °C of T_I. For the other response (MH), the optimal parametric combination that ensured the maximum value of MH was 110 MPa of P_S, 790 °C of T_p, and 246 °C of T_I.
- SEM micrographs of the fractured samples depict that mostly brittle fractures have been observed. Specimens having a maximum value of UTS and MH also demonstrate the brittle fracture along with the flat face morphology. EDX analysis indicates that the insert preheating significantly affects both the UTS and MH.
- Empirical models for the responses UTS and MH have been successfully developed and statistically justified as significant through ANOVA. Results of confirmatory trials have also witnessed the high prediction accuracy of the formulated models. It is pertinent to mention that the magnitude of prediction error for all the eight confirmatory trials was found lesser than 5%.
- The experimental results obtained from optimal parameters depict that accuracy of experimentation through RSM and precision using MO-GA resulted in higher UTS and MH. Moreover, it showed very low deviation from predicted results.

This research work will provide an auspicious approach for foundry men to develop lightweight advanced structural and functional materials with tremendous mechanical characteristics. Moreover, practitioners can utilize the developed empirical models to obtain the desired value of UTS and MH for aged AA2026-AA2026 overcast joints by selecting the optimal combination of input parameters without experimentation.

Open Access This article is licensed under a Creative Commons Attribution 4.0 International License, which permits use, sharing, adaptation, distribution and reproduction in any medium or format, as long as you give appropriate credit to the original author(s) and the source, provide a link to the Creative Commons licence, and indicate if changes were made. The images or other third party material in this article are included in the article's Creative Commons licence, unless indicated otherwise in a credit line to the material. If material is not included in the article's Creative Commons licence and your intended use is not permitted by statutory regulation or exceeds the permitted use, you will need to obtain permission directly from the copyright holder. To view a copy of this licence, visit http://creativecommons.org/licenses/by/4.0/.

References

1. Taub AI, Krajewski PE, Luo AA, Owens JN (2007) The evolution of technology for materials processing over the last 50 years: the automotive example. JOM 59(2):48–57
2. Raza MH, Sajid M, Wasim A, Hussain S, Jahanzaib M (2019) Modeling of the mechanical properties of directionally solidified Al-4.3% Cu alloy using response surface methodology. Int J Adv Manuf Technol:1–13
3. Zhang H, Chen Y, Luo AA (2014) A novel aluminum surface treatment for improved bonding in magnesium/aluminum bimetallic castings. Scr Mater 86:52–55
4. Lee T, Lee Y, Park K, Nersisyan H, Jeong H, Lee J (2013) Controlling Al/Cu composite diffusion layer during hydrostatic extrusion by using colloidal Ag. J Mater Process Technol 213(3):487–494
5. Honarpisheh M, Asemabadi M, Sedighi M (2012) Investigation of annealing treatment on the interfacial properties of explosive-welded Al/Cu/Al multilayer. Mater Des 37:122–127
6. Chang C, Chou C, Hsu S, Hsiung G, Chen J (2010) Effect of laser welding on properties of dissimilar joint of Al-Mg-Si and Al-Mn aluminum alloys. J Mater Sci Technol 26(3):276–282
7. Xue P, Ni D, Wang D, Xiao B, Ma Z (2011) Effect of friction stir welding parameters on the microstructure and mechanical properties of the dissimilar Al–Cu joints. Mater Sci Eng A 528(13–14):4683–4689
8. Chang S, Tsao L, Li T, Chuang T (2009) Joining 6061 aluminum alloy with Al–Si–Cu filler metals. J Alloys Compd 488(1):174–180
9. Lee K, Lee S, Sung H, Lee D, Kim J, Chang Y, Lee S, Kwon Y (2013) Influence of reduction ratio on the interface microstructure and mechanical properties of roll-bonded Al/Cu sheets. Mater Sci Eng A 583:177–181
10. Liu T, Wang Q, Sui Y, Wang Q, Ding W (2016) An investigation into interface formation and mechanical properties of aluminum–copper bimetal by squeeze casting. Mater Des 89:1137–1146
11. Feng J, Ye B, Zuo L, Wang Q, Wang Q, Jiang H, Ding W (2017) Bonding of aluminum alloys in compound casting. Metall Mater Trans A 48(10):4632–4644
12. Yu Z, Duan Y, Liu L, Liu S, Liu X, Li X (2009) Growth behavior of Cu/Al intermetallic compounds in hot-dip aluminized copper. Surf Interface Anal 41(5):361–365
13. Wang T, Liang C, Chen Z, Zheng Y, Kang H, Wang W (2014) Development of an 8090/3003 bimetal slab using a modified direct-chill casting process. J Mater Process Technol 214(9):1806–1811
14. Hu Q, Jiang Z, Jiang W, Li G, Guan F, Jiang H, Fan Z (2019) Interface characteristics of Mg/Al bimetal produced by a novel liquid-liquid compound casting process with an Al interlayer. Int J Adv Manuf Technol 101(5–8):1125–1132
15. Sun J, Song X, Wang T, Yu Y, Sun M, Cao Z, Li T (2012) The microstructure and property of Al–Si alloy and Al–Mn alloy bimetal prepared by continuous casting. Mater Lett 67(1):21–23
16. Hajjari E, Divandari M, Razavi S, Emami S, Homma T, Kamado S (2011) Dissimilar joining of Al/Mg light metals by compound casting process. J Mater Sci 46(20):6491–6499
17. Papis K, Hallstedt B, Löffler JF, Uggowitzer PJ (2008) Interface formation in aluminium–aluminium compound casting. Acta Mater 56(13):3036–3043
18. Papis K, Löffler JF, Uggowitzer PJ (2010) Interface formation between liquid and solid Mg alloys—an approach to continuously metallurgic joining of magnesium parts. Mater Sci Eng A 527(9):2274–2279
19. Ali MA, Jahanzaib M, Wasim A, Hussain S, Anjum NA (2018) Evaluating the effects of as-casted and aged overcasting of Al-Al joints. Int J Adv Manuf Technol 96(1–4):1377–1392
20. Hajjari E, Divandari M, Razavi S, Homma T, Kamado S (2012) Intermetallic compounds and antiphase domains in Al/Mg compound casting. Intermetallics 23:182–186
21. Jiang W, Li G, Fan Z, Wang L, Liu F (2016) Investigation on the interface characteristics of Al/Mg bimetallic castings processed by lost foam casting. Metall Mater Trans A 47(5):2462–2470
22. Hejazi MM, Divandari M, Taghaddos E (2009) Effect of copper insert on the microstructure of gray iron produced via lost foam casting. Mater Des 30(4):1085–1092
23. Zhang H, Chen Y, Luo AA (2014) Improved interfacial bonding in magnesium/aluminum overcasting systems by aluminum surface treatments. Metall Mater Trans B 45(6):2495–2503
24. Jiang W, Fan Z, Li G, Liu X, Liu F (2016) Effects of hot-dip galvanizing and aluminizing on interfacial microstructures and mechanical properties of aluminum/iron bimetallic composites. J Alloys Compd 688:742–751
25. Jiang W, Li G, Wu Y, Liu X, Fan Z (2018) Effect of heat treatment on bonding strength of aluminum/steel bimetal produced by a compound casting. J Mater Process Technol 258:239–250
26. Rübner M, Günzl M, Körner C, Singer R (2011) Aluminium–aluminium compound fabrication by high pressure die casting. Mater Sci Eng A 528(22–23):7024–7029
27. Koerner C, Schwankl M, Himmler D (2014) Aluminum–aluminum compound castings by electroless deposited zinc layers. J Mater Process Technol 214(5):1094–1101
28. Arulraj M, Palani P (2018) Parametric optimization for improving impact strength of squeeze cast of hybrid metal matrix (LM24–SiC p–coconut shell ash) composite. J Braz Soc Mech Sci Eng 40(1):2
29. Concer D, Marcondes P (2017) Experimental and numerical simulation study of porosity on high-pressure aluminum die casting process. J Braz Soc Mech Sci Eng 39(8):3079–3088
30. Lee S, Sohn K-S, Park I-M, Cho K-M (1995) Effect of applied pressure on mechanical properties of squeeze cast mg matrix composites. Met Mater Int 1(1):37–46
31. Liu T, Wang Q, Sui Y, Wang Q (2016) Microstructure and mechanical properties of overcast 6101–6101 wrought Al alloy joint by squeeze casting. J Mater Sci Technol 32(4):298–304
32. Liu T, Wang Q, Sui Y, Wang Q, Ding W (2015) An investigation into aluminum–aluminum bimetal fabrication by squeeze casting. Mater Des 68:8–17
33. Xu G, Luo AA, Chen Y, Sachdev AK (2014) Interfacial phenomena in magnesium/aluminum bi-metallic castings. Mater Sci Eng A 595:154–158
34. Liu G, Wang Q, Liu T, Ye B, Jiang H, Ding W (2017) Effect of T6 heat treatment on microstructure and mechanical property of 6101/A356 bimetal fabricated by squeeze casting. Mater Sci Eng A 696:208–215
35. Li G, Jiang W, Fan Z, Jiang Z, Liu X, Liu F (2017) Effects of pouring temperature on microstructure, mechanical properties, and fracture behavior of Al/Mg bimetallic composites produced

by lost foam casting process. Int J Adv Manuf Technol 91(1–4): 1355–1368
36. S-b B, S-m X, Ning Z, Lan L (2013) Influence of technical parameters on strength and ductility of AlSi9Cu3 alloys in squeeze casting. Trans Nonferrous Metals Soc China 23(4):977–982
37. Chen G, Chang X, Zhang J, Jin Y, Sun C, Chen Q, Zhao Z (2019) Microstructures and mechanical properties of in-situ Al 3 Ti/2024 aluminum matrix composites fabricated by ultrasonic treatment and subsequent squeeze casting. Met Mater Int 1–11
38. Saito M, Maegawa T, Homma T (2005) Electrochemical analysis of zincate treatments for Al and Al alloy films. Electrochim Acta 51(5):1017–1020
39. Teng L, Wang Q-d, Ping L, J-w S, X-l Y, Wang Q-g (2015) Microstructure and mechanical properties of overcast aluminum joints. Trans Nonferrous Metals Soc China 25(4):1064–1072
40. Zhang Y, Ji S, Scamans G, Fan Z (2017) Interfacial characterisation of overcasting a cast Al-Si-Mg (A356) alloy on a wrought Al-Mg-Si (AA6060) alloy. J Mater Process Technol 243:197–204
41. Souissi N, Souissi S, Lecompte J-P, Amar MB, Bradai C, Halouani F (2015) Improvement of ductility for squeeze cast 2017 a wrought aluminum alloy using the Taguchi method. Int J Adv Manuf Technol 78(9–12):2069–2077
42. Haider KMA, Mufti NA (2014) Mechanical and microstructural evaluation of squeeze cast Al-4% Cu alloy using a full-factorial experimental design. JOM 66(8):1446–1453
43. Raza MH, Wasim A, Ali MA, Hussain S, Jahanzaib M (2018) Investigating the effects of different electrodes on Al6061-SiC-7.5 wt% during electric discharge machining. Int J Adv Manuf Technol 99(9–12):3017–3034
44. Oh JS, Nam H-S, Choi J-H, Lee S-C (2013) Prediction of atomic structure of Pt-based bimetallic nanoalloys by using genetic algorithm. Met Mater Int 19(3):513–518
45. Patel GM, Mathew R, Krishna P, Parappagoudar MB (2014) Investigation of squeeze cast process parameters effects on secondary dendrite arm spacing using statistical regression and artificial neural network models. Procedia Technol 14:149–156
46. Park Y, Cho H (2005) A fuzzy logic controller for the molten steel level control of strip casting processes. Control Eng Pract 13(7): 821–834
47. Ali MA, Ishfaq K, Jawad M (2019) Evaluation of surface quality and mechanical properties of squeeze casted AA2026 aluminum alloy using response surface methodology. Int J Adv Manuf Technol 1–14
48. Moradi M, Meiabadi S, Kaplan A (2019) 3D printed parts with honeycomb internal pattern by fused deposition modelling; experimental characterization and production optimization. Met Mater Int 1–14
49. Sarfraz MH, Jahanzaib M, Ahmed W, Hussain S (2019) Multi-response parametric optimization of squeeze casting process for fabricating Al 6061-SiC composite. Int J Adv Manuf Technol 102(1–4):759–773
50. Lee J, Kim H, Won C, Cantor B (2002) Effect of the gap distance on the cooling behavior and the microstructure of indirect squeeze cast and gravity die cast 5083 wrought Al alloy. Mater Sci Eng A 338(1–2):182–190
51. Nerl C, Wimmer M, Hoffmann H, Kaschnitz E, Langbein F, Volk W (2014) Development of a continuous composite casting process for the production of bilayer aluminium strips. J Mater Process Technol 214(7):1445–1455

Publisher's note Springer Nature remains neutral with regard to jurisdictional claims in published maps and institutional affiliations.